

Rise and fall of a multicomponent droplet in a surrounding fluid: simulation study of a bumpy path

Mirantsoa Aimé Rasolofomanana

*CEA, DES, IRESNE, DTN, St Paul-Lez-Durance 13108, France and
Laboratoire de Physique de la Matière Condensée,
Institut Polytechnique de Paris, CNRS, Palaiseau 91120, France*

Romain Le Tellier

CEA, DES, IRESNE, DTN, St Paul-Lez-Durance 13108, France

Hervé Henry

*Laboratoire de Physique de la Matière Condensée,
Institut Polytechnique de Paris, CNRS, Palaiseau 91120, France*

(Dated: April 1, 2024)

The coupling between mass transfer and hydrodynamic phenomena in two-phase flow is not necessarily straightforward due to the different effects that can be encountered. The treatment of such coupling is complex and requires particular efforts, especially in the modelling of the interface between phases. In this paper, we consider the case of a droplet composed of two components (one miscible and one immiscible in water) released in a 2D rectangular domain filled with water. Mass transfer occurs between the miscible element and the surrounding water, which leads to a density inversion that directly affects the droplet trajectory through buoyancy. We perform simulations using a ternary Cahn-Hilliard model (implemented in the “phase_field” model of the TrioCFD code) to capture such coupled phenomena. The Boussinesq approximation for a multicomponent system is used to define the density law and an analytical chemical potential is proposed for the thermodynamic landscape. The effect of the mobility parameter on the flow is highlighted and the results found are in good agreement with the dynamics described from an experimental study of the open literature.

I. INTRODUCTION

Multiphase flows are ubiquitous and can be seen in industrial processes and natural environment. They are difficult to describe and model numerically due to the coupling between the moving free surface and the fluid flow. This leads to complex behaviours that are still a challenge to describe and they are therefore driving new development in modelling. This complexity may be augmented when mass transfer between the two phases can occur. This is typically the case in industrial flows and mixing. For instance, such phenomena take place in the corium pool after a severe nuclear accident and affect thermal transfers [1–3]. Such mass transfer can also occur in microfluidic devices [4] and also during the geological sequestration of CO₂ either in coal or in deep aquifers [5, 6]. Finally, they are of importance in industrial processes where the dispersion of chemical components in a surrounding fluid is mediated by the motion of droplets [7].

In such a situation, mass transfer will occur between the two phases and will affect the fluid flow. This was exemplified in a recent experimental work [8] inspired by oil spills. Here, through numerical simulations, we show the ability of a ternary phase field model to describe the complex interplay of mass transfer through diffusion and flow equation in the presence of buoyant force. To this purpose, we compare numerical results obtained with a recent experimental work in a qualitative manner. The numerical results also show that the difference between a *naive* description of the motion and the fully coupled problem can be dramatic and can be well explained by the analysis of the solution of the fully coupled problems. This illustrates the need for fully coupled simulations of such systems. Indeed, while multiphase flows are ubiquitous, simulations methods such as volume of fluids [9] or level set usually rely on the assumption that both phases are immiscible and that no mass transfer should occur through the interface [10]. Phase field models based on either the Allen-Cahn [11, 12] or the Cahn-Hilliard model [13–15] can obviously describe mass transfer through the interface. However, this possibility has not been used fully explored and is seen as an adverse effect when modelling multiphase flows of perfectly immiscible fluids [16, 17]. Here, we show that a ternary Cahn-Hilliard model coupled with the Navier-Stokes equations, using a simple free energy functional is able to describe the complex interplay between fluid flow and diffusive transport and that such modelling effort brings new insights. This is exemplified by numerical simulations of the motion of a multicomponent droplet moving into water while one of its components diffuses out of the droplet leading to changes in the droplet buoyancy. The numerical results are compared to experimental results presented in [8].

The paper is organised as follows. First, we briefly describe the phenomena at play in the experiment of interest and discuss qualitatively why a proper description of the coupling between mass transfer and hydrodynamics is needed. Then, we describe the generic form of the model and the simulation setup. Thereafter, we present numerical simulation results that show the ability of the model to describe the interplay between hydrodynamics and mass transfer phenomena before drawing a conclusion and some perspectives.

II. DESCRIPTION OF THE MODEL

The dynamics of a multicomponent droplet released in a quiescent water column is studied experimentally in [8]. The droplet is initially composed of two components: one (denoted A) with a density lower than of water is miscible with water, the other (denoted B) with a density larger than of water is not. For some compositions of the droplet, the following sequence is observed: first, the droplet rises in the water and slows down until it reaches zero velocity and finally sinks with an increasing velocity until a limiting velocity is reached. This can be well explained qualitatively by the evolution of the composition of the droplet due to diffusion.

Indeed, if the droplet composition is sufficiently rich in the light element, it becomes lighter than water and will move up. However, due to diffusion of the miscible element in water, the amount of A in the droplet will decrease while the amount of heavy element B remains constant. As a result, the density of the droplet

will increase until it reaches the density of pure B which is heavier than water. This implies that the density of the droplet that was initially less than water increases, becomes equal to that of the surrounding water and eventually is larger, resulting in the observed motion.

This explanation is fairly simple, however, if one wants to reproduce this behaviour quantitatively, which may be of interest for instance when modelling flow patterns in corium [1], the crude approximation where the diffusive mass transfer is computed considering a droplet in pure water and then the motion of the droplet is obviously incorrect, since it neglects the diffusion layer that builds around the droplet. In the same spirit, considering that the mass transfer is the same as for a quiescent droplet is incorrect, since it neglects the advection that affects the composition around the droplet. Therefore, in order to reproduce quantitatively such motion, one needs to solve the fully coupled problem: the advection-diffusion equation together with the Navier-Stokes equations. This can be done with numerical simulations using the phase field method [14, 15, 18, 19]. This class of models relies on a diffuse interface that can be tracked implicitly and has been used to model multiphase flows but rarely to model diffusive transport coupled with flow while it has been shown to be efficient [20].

It presents the advantage of being thermodynamically consistent: by construction, it derives from a free energy functional (the thermodynamic landscape). In addition, it is fairly simple to implement since it is solely based on coupled PDEs discretised over an Eulerian spatial mesh. Nevertheless, the thermodynamic landscape and model parameters must be chosen with care to give the desired properties. For instance, the diffuse interface thickness is given by a balance between the thermodynamic landscape and the magnitude of a squared gradient term. The accuracy of the model when considering simple multiphase flows has been shown to depend on the mobility of chemical species [16, 17]. In the more complex case of ternary system, additional interface properties, such as adsorption, have been shown to be difficult to control [21] for thermodynamic landscapes obtained from thermodynamic databases such as the ones constructed by the popular Calphad method [21, 22].

In the present paper, we use the phase field model to study numerically the dynamics of a multicomponent droplet in water. Based on so-called diffuse interface approach, the properties in the phase field model are described by ϕ_k called ‘‘order parameters’’ which take on two different constant values in each phase and vary continuously within the interface. The diffuse interface description was originally proposed by Van der Waals [23], it was then popularised by Cahn [13] in the context of diffusive mass transfer. It has been then used to describe the motion of free interfaces in a natural way [24, 25] in the context of solid growth where it has become a standard approach [26, 27]. It has been extended thereafter to fluid flow using either a conserved order parameter [11] or a non-conserved order parameter [12]. Here, since the diffusion of chemical species in a ternary system is considered, we used a conserved approach that allows a simple use of ternary system [15] that has already been used in other contexts [20]. In an effort to describe systems of interest, there has been recent efforts to couple the principle of such diffuse interface model with free energy functional extracted from thermodynamic databases [21, 28]. In this paper, we focus on the description of the interplay between diffusive mass transport and fluid flow. Therefore, we have chosen more standard free energy functionals that are prone to very little interface adsorption.

In this work, we consider 3 order parameters that represent the component volume fractions *i.e.* element A, element B and water and assume that the molar volume is constant for each element. In a ternary system, the evolution of these conserved order parameters ϕ_i for $i \in \{A, B\}$ are governed by the advective Cahn-Hilliard equations:

$$\begin{aligned} \frac{\partial \phi_i}{\partial t} + \mathbf{u} \cdot \nabla \phi_i &= \nabla \cdot \left(\sum_{j \in \{A, B\}} \mathcal{M}_{i,j} \nabla \tilde{\mu}_j \right) \\ \tilde{\mu}_i &= \lambda \frac{\partial G}{\partial \phi_i} - \sum_{j \in \{A, B\}} \kappa_{i,j} \Delta \phi_j \end{aligned} \quad (1)$$

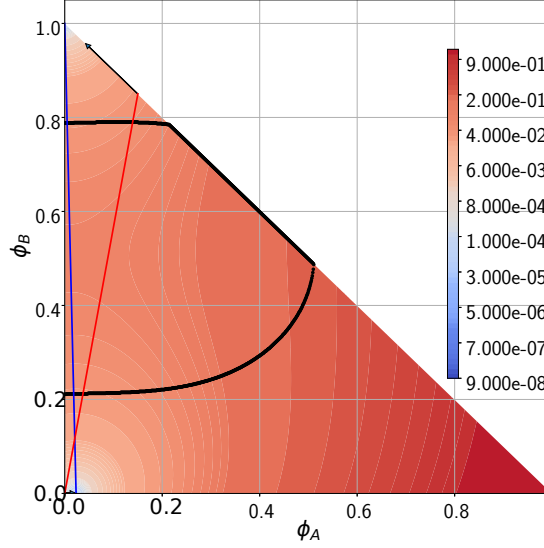


FIG. 1. Thermodynamic landscape represented in the energy surface of the free energy density G shown on logarithmic scale. The blue line is the tie-line, the red one connects the compositions at initial state and the black line represents the spinodal curve.

with \mathbf{u} the advective velocity field, $\tilde{\mu}_j$ the chemical potential of the element j , G the double-well free energy, the mobility $\mathcal{M}_{i,j}$, the gradient energy $\kappa_{i,j}$ and λ an upscaling parameter [21, 28] defined later. The gradient coefficient matrix is chosen simply to be

$$\bar{\bar{\kappa}} = \begin{bmatrix} \kappa^{bin} & 0 \\ 0 & \kappa^{bin} \end{bmatrix} \quad (2)$$

where κ^{bin} is the gradient energy coefficient obtained from a binary system. The coefficients of the mobility matrix are taken simply to be equal to:

$$\bar{\bar{\mathcal{M}}} = \begin{bmatrix} M & 0 \\ 0 & M \end{bmatrix} \quad (3)$$

In this work, M is taken to be equal to: 10^{-8} ; 5×10^{-9} , 2.5×10^{-9} , 1×10^{-9} and $5 \times 10^{-10} J^{-1} m^5 s^{-1}$. We discuss the effect of this parameter on the simulation results in Section IV.

These advective Cahn-Hilliard equations are coupled with the Navier-Stokes equations in order to describe the whole system. Based on the so-called ‘‘one fluid model’’, the phase field model treats the two phases as a single one [29]. Thus, we get the Navier-Stokes equations for a ternary system under the Boussinesq approximation:

$$\rho^* \frac{d\mathbf{u}}{dt} = -\nabla P + \sum_{i \in \{A,B\}} \tilde{\mu}_i \nabla \phi_i + (\rho(\phi_A, \phi_B) - \rho^*) \mathbf{g} + \eta \Delta \mathbf{u} \quad (4)$$

where P is the pressure, η is the dynamic viscosity (taken independent of the chemical composition here), \mathbf{g} is the gravity, the term with $\tilde{\mu}_i$ represents the capillary force within the interface as proposed in [30], ρ^* the

η	10^{-3} Pa.s	σ	0.0036 J.m ⁻²
ε	0.0008 m	λ	5.4 J.m ⁻³
ρ^*	1000 kg.m ⁻³	β_A	-0.416
β_B	0.05	κ^{bin}	4.3210^{-5} J.m ⁻¹
ρ_A	0.584 kg.m ⁻³	ρ_B	1050 kg.m ⁻³

TABLE I. Summary of model parameters.

mass density of reference and ρ is the mass density that is function of the order parameters ϕ_A and ϕ_B and writes, under the assumption of constant molar volume:

$$\begin{aligned}\rho(\phi_A, \phi_B) &= \rho^* \left(1 + \sum_{i \in \{A, B\}} \beta_i \phi_i\right) \\ &= \rho^* (1 + \beta_A \phi_A + \beta_B \phi_B)\end{aligned}\quad (5)$$

with $\rho^* = 1000 \text{ kg/m}^3$, $\beta_A = -0.416$ and $\beta_B = 0.05$.

The chemical potential (Eq. 1) is given by the double-well free energy that is chosen in such a way that at thermodynamic equilibrium, the droplet contains only pure B element and the element A is completely dissolved in the continuous phase. It writes:

$$G = \left[(\phi_A - \phi_A^{eq,cont})^2 + \phi_B^2 \right] \left[(1 - \phi_B)^2 + \phi_A^2 \right] \quad (6)$$

where $\phi_A^{eq,cont}$ is the composition of the element A in the continuous phase at thermodynamic equilibrium which depends on the size of the domain (see Table II). With such a choice of thermodynamic landscape, there exists a region where the homogeneous mixture is unstable (the spinodal domain). It corresponds to the domain for which the Hessian matrix of G has one negative eigenvalue and is represented in fig 1. In this region, small fluctuations of the composition can grow and lead to the formation of domains with different compositions. It should be noted that with this choice of G , no adsorption at the interface between pure B and pure water occurs when using a diagonal $\bar{\kappa}$.

The initial compositions of the droplet and of water $\phi_A^{ini,dis}$ and $\phi_B^{ini,dis}$ must satisfy some conditions. No phase separation should occur during the whole simulation neither in the droplet nor in the bulk phase. Therefore, the initial compositions must be outside the spinodal region and the path between the initial and the equilibrium compositions must not cross it. If $(\phi_A^{ini,dis}, \phi_B^{ini,dis})$ is inside the spinodal region, the droplet will separate immediately. In addition, if $(\phi_A^{ini,dis}, \phi_B^{ini,dis})$ is outside the miscibility gap but on the same side as the equilibrium point of the continuous phase, the system will evolve towards one single-phase system. Consequently, to reproduce the desired dynamics, the initial compositions of the two phases must necessarily lie on both sides of the spinodal region.

Taking these criteria into account, we have chosen a droplet with 85% of element B and 15% of element A. Doing so, the dispersed and continuous phases will reach their respective equilibrium composition following the arrows as shown in Fig. 1. These are obtained from the orientation of the G gradients at the initial composition points. This ensures that no water is introduced into the droplet. With this choice the initial density of the droplet is $\rho_{dis}^{ini} = 980 \text{ kg/m}^3$ (slightly lower than that of water).

III. SIMULATION SETUP

In this work, we use the TrioCFD code, an open-source software, developed by the French Alternative Energies and Atomic Energy Commission (CEA) to treat thermal hydraulics problems [31, 32]. It has been designed to solve different models including the *phase_field* model for multiphase flow where coupled Cahn-Hilliard and Navier-Stokes equations are implemented. It is worth noting that in the official version 1.8.4, only binary system with one equation of Cahn-Hilliard can be solved [33]. For the work presented here, we have extended the capabilities of the *phase_field* application so that it can treat an arbitrary number of components. The numerical results presented here have been shown to be in quantitative agreement with results of simulations using a pseudospectral[34] code that has been proven to be very accurate in the context of binary mixture[17, 35] and that has been extended to ternary mixtures.

The computational domain consists of a 2D rectangular domain of width $L_x = 54 \times 10^{-3}$ m and $L_y = 95 \times 10^{-3}$ m in which a droplet of initial radius of $R = 3.3 \times 10^{-3}$ m is placed far enough from the walls to limit edge effects. The wall boundary condition imposes no slip (both components of velocities are zero) at the lower and upper face of the computational domain.

The viscosity of both phases is $\eta = 10^{-3}$ Pa.s. For such parameter values and a millimetric size droplet moving at velocities of the order of 10^{-2} m/s, the associated Reynolds number is of the order of 10. This implies that inertial effects cannot be neglected. The surface tension is $\sigma = 36 \times 10^{-3}$ N/m as used in [8]. With this value and the properties of the droplet, the Bond Bo and Morton Mo numbers are:

$$Bo = \frac{\Delta\rho g D^2}{\sigma} \quad (7)$$

$$Mo = \frac{g \Delta\rho \eta^4}{(\rho_{cont}^2 \sigma^3)} \quad (8)$$

where $\Delta\rho$ is the density difference between two phases, D is the diameter of the droplet and ρ_{cont} the density of the continuous phase. In our case, we have $Bo \approx 0.1$ and $Mo \approx 10^{-10}$ corresponding to the spherical regime according to Clift's diagram [36].

The uniform mesh size is set to 2×10^{-4} m. As a result there are 4 cells within the interface so that the interface structure can be captured and that grid anisotropy can be neglected. Accordingly, the upscaling parameter λ is introduced in the phase field model in order to treat a larger interface thickness than the characteristic length scale of the physical interface [21, 28]. With such a thermodynamic landscape and the related equilibrium compositions, the parameters κ^{bin} and λ can be defined from the surface tension σ and interface thickness ε as:

$$\kappa^{bin} = \frac{3}{2} \sigma \varepsilon \quad (9)$$

$$\lambda = 12 \frac{\sigma}{\varepsilon} \quad (10)$$

The initial condition is a quiescent droplet with composition:

$$\phi_i(x, y, t = 0) = \frac{\phi_i^{ini,dis}}{2} \left(1 - \tanh \left(\frac{\sqrt{(x-x_0)^2 + (y-y_0)^2} - R}{\varepsilon} \right) \right) \quad (11)$$

with R the radius of the circular droplet, ε the interface thickness, (x_0, y_0) the coordinates of the center of the droplet in the 2D domain and $\phi_i^{ini,dis}$ is the composition of the element $i \in \{A, B\}$ in the dispersed phase

TABLE II. Summary of the compositions of elements A and B with the density of each phase at initial and equilibrium states.

phase	initial state	equilibrium state
dispersed	$\phi_A^{ini,dis} = 0.15$	$\phi_A^{eq,dis} = 0$
phase	$\phi_B^{ini,dis} = 0.85$	$\phi_B^{eq,dis} = 1$
(droplet)	$\rho_{dis}^{ini} = 980\text{kg.m}^{-3}$	$\rho_{dis}^{eq} = 1050\text{kg.m}^{-3}$
continuous	$\phi_A^{ini,cont} = 0$	$\phi_A^{eq,cont} = \frac{\phi_A^{ini,dis} V_{dis}^{ini}}{V_{tot} + (\phi_A^{ini,dis} - 1) V_{dis}^{ini}}$
phase	$\phi_B^{ini,cont} = 0$	$\phi_B^{eq,cont} = 0$
	$\rho_{cont}^{ini} = 999.5\text{kg.m}^{-3}$	$\rho_{cont}^{eq} = \rho_{wat} \left(1 + \beta_A \phi_A^{eq,cont} \right)$

at initial state. With this choice of initial condition, assuming that the final droplet is composed of pure B [37], we expect that the final volume of the droplet will be $(1 - \phi_A^{ini,dis})V_{dis}^{ini}$ with V_{dis}^{ini} the initial volume of the droplet (the Gibbs Thomson effect is neglected here). The properties of each phase are shown in Table II. In addition other model parameters are summarized in Table I.

Before turning to the result, we find necessary to discuss how some quantities related to the droplet are computed. Indeed, since there is practically no mass transfer of immiscible element to the continuous phase, we are particularly interested in the amount of immiscible element in presence. Thus, we can define the position of the droplet from the position of the center of mass and its velocity by:

$$\mathbf{x}_G = \frac{\int \mathbf{x} \phi_B}{\int \phi_B} \quad (12)$$

$$\mathbf{u}_G = \frac{\int \mathbf{u} \phi_B}{\int \phi_B} \quad (13)$$

where ϕ_B is the molar fraction of the immiscible component, $\mathbf{x}(x, y)$ and \mathbf{u} are the spatial coordinates and velocities of a point.

IV. RESULTS AND DISCUSSION

We now present numerical results obtained with this model and discuss them. First, we present the results from a qualitative point of view. Second, we discuss the interplay between diffusive mass transport and advection and show that it has significant effects on the droplet dynamic that can not be neglected. This emphasises the importance of fully coupled numerical simulations as the one presented here.

A. General behaviour

As expected, calculations show that x_G remains constant throughout the simulation. That implies that the droplet follows a rectilinear trajectory as shown in fig 2 where the position of the droplet along the vertical axis y is plotted as a function of time for different values of M . Its trajectory includes an ascending phase followed by a descending phase. In the ascending phase, the droplet being lighter than the surrounding water first starts to rise. In the same time, the miscible component of the droplet diffuses out in water, resulting in an increase of the droplet density. After a while, the droplet reaches a maximum height, becomes heavier than the continuous phase and ends up falling down into the water. This behaviour is in good qualitative

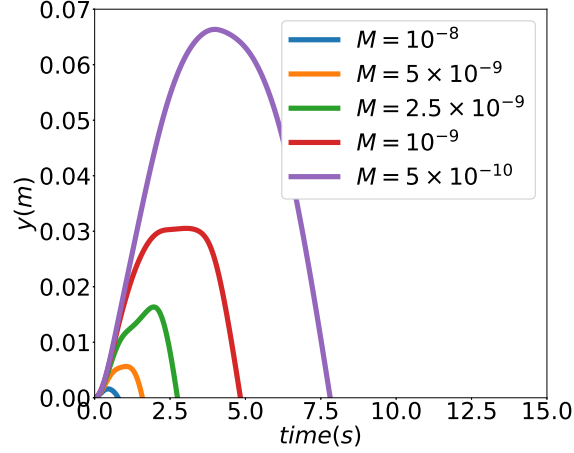


FIG. 2. Position of the droplet as a function of time for different values of the mobility.

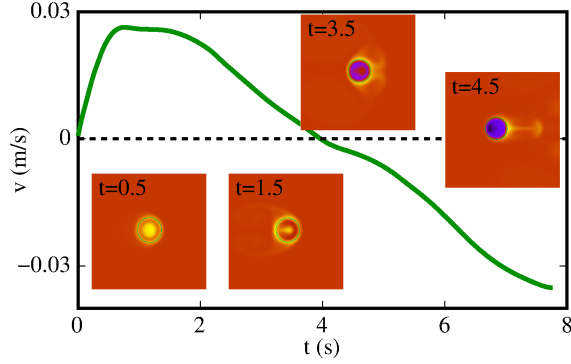


FIG. 3. Typical evolution of the droplet velocity as a function of time where the density maps are also shown at different times. The mobility is $5 \cdot 10^{-9}$.

agreement with experimental results presented in [8] and is robust to changes in parameters such as the mobility. However, one can see that changes in the mobility dramatically affect the amplitude and duration of its motion. For instance, for $M = 10^{-8} J^{-1} m^5 s^{-1}$, the amplitude of the droplet motion is $\sim R/2$ (R is the radius of the droplet) while for $M = 5 \times 10^{-10} J^{-1} m^5 s^{-1}$, it corresponds to $\sim 20R$. This is consistent with the fact that the characteristic diffusion time τ obtained by scaling the Cahn-Hilliard equations is proportional to the inverse of the mobility *i.e.* $\tau \sim \frac{1}{M}$. For lower mobilities, the diffusion is slower. Hence, the droplet rises high enough. On the contrary, when mobility M is greater, the diffusion becomes faster and the droplet is unable to reach the same height.

In order to analyse the droplet motion, in the following, we will use the droplet velocity evolution curve that allows a better analysis. Therefore, we first give a qualitative description of the evolution of the droplet velocity.

A typical curve of the velocity along the vertical axis together with maps of the density at given times is presented in Fig. 3 for $M = 5 \times 10^{-9} J^{-1} m^5 s^{-1}$. One can see that after an acceleration phase that is

absent from experimental curves in [8], the velocity of the droplet reaches a maximum and starts to decrease linearly (with a few bumps) until it reaches a limiting velocity. When looking at the density map, with the exception of the initial map, the boundary between the droplet and the continuous phase appears clearly (in supplemental material we present the corresponding maps of all fields for the cases presented here at different times). It can be seen at the two intermediate steps that there is a light fluid layer (A rich without any B) around the droplet that is *attached* to the droplet when the droplet velocity is maximum and that has partially detached from the droplet when its vertical velocity cancels.

It is worth mentioning that when the droplet velocity is at its maximal value, the droplet density is already larger than the density of water which is unexpected. This can be explained by two facts. First, inertia introduces a delay (this will be discussed in the next section), second, if one consider the volume occupied by the droplet and the surrounding diffusive layer, its average density is the average density of the initial droplet and of the surrounding pure water. Since the initial droplet was lighter than water, this average density is smaller than the density of water and this *virtual* volume of fluid is pushed upward by buoyant forces.

Thereafter, the droplet velocity decreases, but the droplet is still rising. One can see that the surrounding layer of light fluid has detached from the droplet due to buoyant forces. At this stage, the droplet is significantly denser than water and its velocity cancels. The droplet falls in the fluid leaving behind a plume of A rich water until the droplet is composed of pure B and reaches a limiting velocity.

These observations already illustrate the interplay between diffusion and flow. Indeed, one can see that the droplet density is asymmetric and that it is denser in its lower part. This is related to the fact that, as can be seen on the map, the diffusive layer is thinner at the bottom of the droplet than at its top. This leads to a more efficient diffusive transport of A out of the droplet, a faster decrease in A at the bottom of the droplet, which translates into a heavier fluid. This configuration is stable with respect to buoyant forces, however, its origin comes from the interplay of diffusion and flow and not some sedimentation.

In the following section, the effect of the mobility on the droplet motion is discussed.

B. Effect of the mobility

In the case of a quiescent droplet, the evolution of its composition is governed by Eq. 1 with the mobility \bar{M} given by Eq. 3 and a velocity $\mathbf{u} = 0$. It can be rewritten as

$$\frac{1}{M} \frac{\partial \phi_i}{\partial t} = \nabla \cdot (\nabla \bar{\mu}_i) \quad (14)$$

and $1/M$ is proportional to the characteristic time of evolution of the composition of the droplet. This implies that for a quiescent droplet with varying values of M , the exact same behaviour is expected after a rescaling of time by $1/M$. Since the droplet motion affects the diffusion, we do not expect this scaling to hold strictly speaking. However, for high values of the mobility (for low values of the buoyant forces, which is not studied here, this scaling is also valid), it should be the main effect of mobility. Since inertial effects cannot be neglected, we do not expect that the curves of velocity as a function of rescaled time superimpose for high values of mobility. This is indeed the case, as can be seen in Fig. 4 where the droplet velocity is plotted as a function of the time rescaled by M .

Before discussing the results and the peculiar shape of the curves, we discuss a simple phenomenological model that aims at putting under light the simple effects of both inertia and diffusive transport. To this purpose, we consider a simple model of the droplet motion:

$$m \frac{du}{dt} = f(Mt) - \lambda u \quad (15)$$

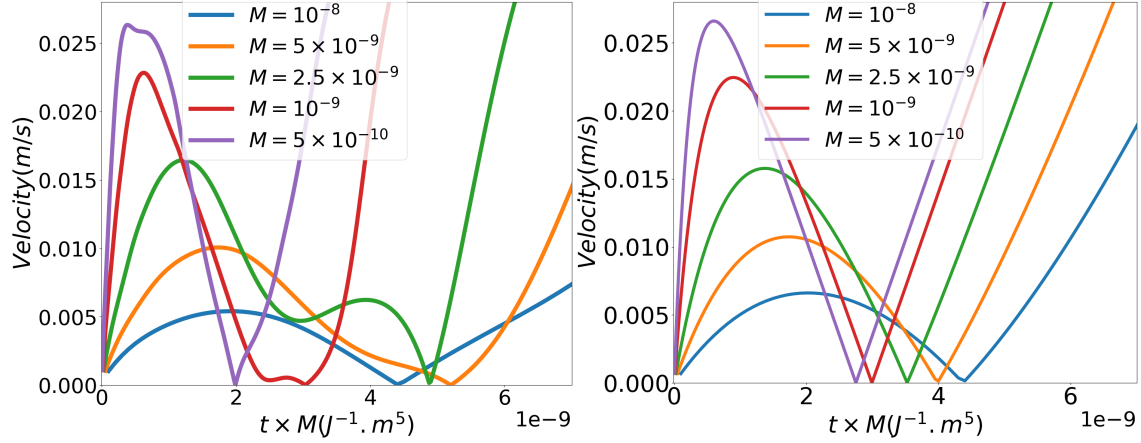


FIG. 4. **left** Absolute velocity of the droplet for different mobilities with respect to time \times mobility. **right** velocity curves obtained using the reduced model.

where m is an effective mass, $f(Mt)$ is a function that describes the effect of buoyant forces and that evolves due do diffusive process and λ is an effective friction. We consider the simple case where $f(t) = a(1 - t/t_0)$. Taking into account the initial condition $u(0) = 0$, this simple model can be solved analytically and has for solution

$$u(t) = \frac{a}{\lambda} \left[\left(1 + \frac{mM}{\lambda \xi_0} \right) \left(1 - e^{-\lambda t/m} \right) - \frac{Mt}{\xi_0} \right] \quad (16)$$

Using $a = 0.035\text{m/s}$, $\xi_0 = 2.5 \times 10^{-9}\text{J}^{-1}\text{m}^5$, $m = 0.04\text{kg}$ and $\lambda = 0.08\text{kg/s}$, one can get the curves presented in Fig. 4. Parameters were chosen so that the time at which the velocity cancels for the highest mobility is approximately the same as in numerics and the peak velocity for the lowest mobility is also in agreement with numerics. It must be noted that with such values of the parameters, the buoyant force changes sign at $t \times M = 2.5 \times 10^{-9}\text{J}^{-1}\text{m}^5$ in the model. In the curve obtained with the model for the two lowest mobilities, the velocity changes sign at $t \times M \approx 2.5 \times 10^{-9}$, indicating that in these two cases, once the initial acceleration phase is over, the driving force time scale is larger compared to the inertial time scale, so that the later can be neglected. On the opposite, for $M = 10^{-8}\text{J}^{-1}\text{m}^5\text{s}^{-1}$, the maximum of the velocity corresponds to $t \times M \approx 2.5 \times 10^{-9}$.

When comparing with reduced model results, one can see that the general shape of the velocity curve is in good agreement with numerics and the general qualitative behaviour is recovered. However, in the case of low mobility values, a few differences can be seen.

For $M = 5 \times 10^{-10}\text{J}^{-1}\text{m}^5\text{s}^{-1}$, one can see that the main difference is that the time at which the velocity cancels is slightly smaller in the numerics than in the reduced model. This difference is of the order of approximately 20% and is related to the advective transport of the A component leading to a faster evolution. In addition, one can see a small bump in the numerical velocity curve close to its maximum. This aforementioned velocity bump is also present (and much more visible since it translates into a well marked velocity *plateau*) in numerical results for $M = 1, 2.5$ and $5 \times 10^{-9}\text{J}^{-1}\text{m}^5\text{s}^{-1}$. We give a rationale for these two effects in the following.

First, the *fastest* evolution of the droplet velocity for small values of M can be attributed to the fact that due to the advection, the droplet is moving in fresh water. As a result, the diffusion layer is small and the diffusive

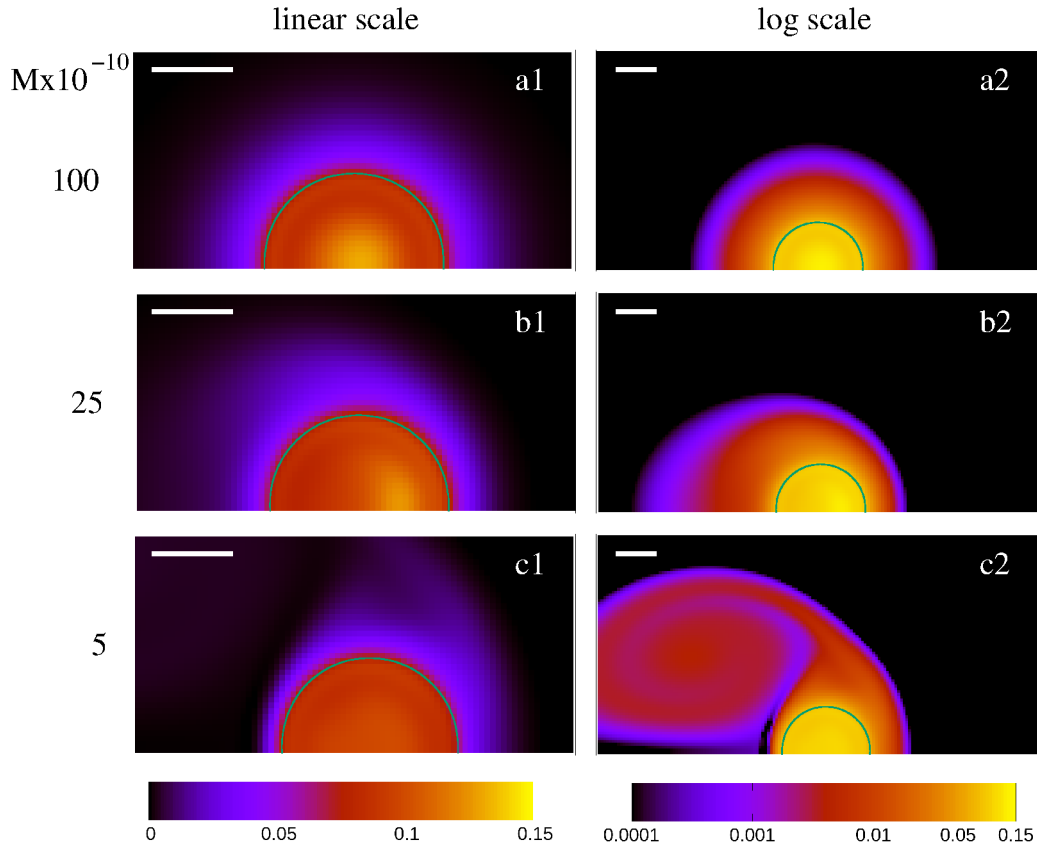


FIG. 5. Molar fraction field of the element A at $t \times M = 1.5 \times 10^{-9} J^{-1} m^5 s^{-1}$ for different mobilities M using either a linear scale (first column) or a logarithmic scale (rightmost column). The bubble defined as an isoline of B element is drawn and the scale between the columns is not the same. The white bar corresponds to $\approx 3 \text{ mm}$. Only a portion of the domain is shown in both cases.

transport is fast, leading to a faster transport of A outside of the droplet. This can be seen in Fig. 5 where the composition map of A is represented for different values of M at rescaled time $M \times t = 10^{-9} J^{-1} m^5$. Regardless of M ($M \in [5 \times 10^{-10}, 10^{-8}] J^{-1} m^5 s^{-1}$), the droplet is in its ascending phase at this value of $M \times t$. However, the distribution of the miscible element in the droplet and its diffusion in water are different depending on the value of M . For larger values of M (*i.e.* $M = \{5 \times 10^{-9}, 10^{-8}\} J^{-1} m^5 s^{-1}$), the diffusion dominates and the droplet behaves in almost the same way for these two values. On the other hand, its behaviour is significantly different for the lowest mobilities $M \leq 2.5 \times 10^{-9} J^{-1} m^5 s^{-1}$ where diffusion is slower. The diffusion field is then modified by the flow. This can be seen in Fig. 5 where the volume fraction of element A is represented using pseudo colors at $t \times M = 1.5 \times 10^{-9} J^{-1} m^5$ for different mobilities using both linear and logarithmic scales. One can clearly see that the extent of the diffusion layer is asymmetrical in the low mobility case (b1 and c1) while it has almost cylindrical symmetry in the high mobility case (a1). In addition, using the linear scale, one can see that, the diffusion layer is thinner both ahead and behind the droplet leading to faster diffusive transfer for low mobilities.

Second, we discuss the presence of a *plateau* in the velocity curve for small values of the mobility. Since

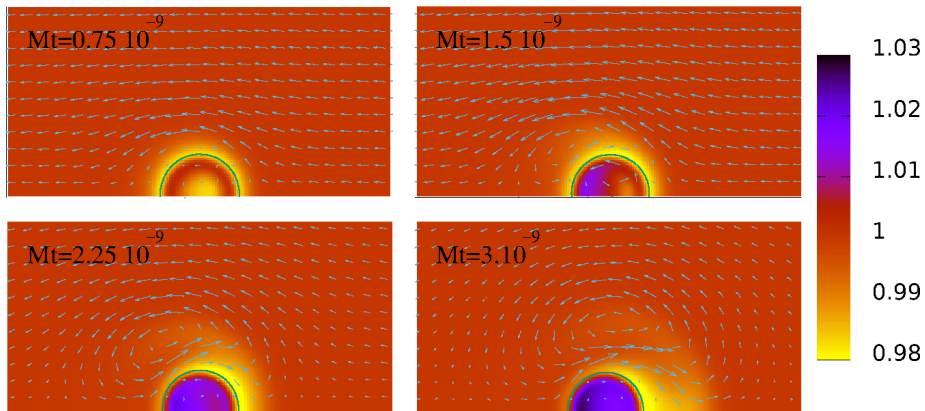


FIG. 6. Velocity vectors in the frame of the droplet in the density field for $M = 2.5 \times 10^{-9} J^{-1} m^5 s^{-1}$ at different times that correspond to the bump in the velocity field. Light regions are represented in yellow while dense regions in red-purple. Pure water density is orange. Only a portion of the domain is shown.

it is well marked for $M = 2.5 \times 10^{-9} J^{-1} m^5 s^{-1}$ we will focus on this case. First one should notice it has significant consequences: the rescaled time at which the droplet starts to sink (cancellation of the velocity) is significantly larger than in the high mobility case while, as explained above, the advection alone would lead to an earlier descent. The plot of the velocity field in the frame of the droplet (that is the velocity field in the laboratory frame minus the average velocity of the droplet) together with the fluid density in Fig. 6 allows to better understand this phenomenon. All plots correspond to the ascending phase. The first one is well before the bump and one can see a droplet moving in a flow that is very similar to a Stokes flow around an obstacle (the droplet is moving from left to right). The second one corresponds to a time close to the onset of the plateau and one can see that next to the droplet, there is a boundary layer close to the droplet that is moving faster than it in the same direction. It corresponds to the region of the surrounding fluid that is rich in A element and is lighter and it induces a viscous force in the same direction as the droplet motion. For later times, this effect is stronger, however, one can see that the light region is moving slowly toward the front of the droplet and eventually detaches from the droplet, leading to the end of the plateau. This effect is similar to the drafting technique in a peloton [38, 39].

The further evolution of the droplet is simple, it keeps losing A component until it reaches a terminal velocity that corresponds to the Stokes velocity of a droplet of pure B in a water bath.

V. CONCLUSION

We have carried out a 2D simulation of the dynamics of a multicomponent droplet released in a water column using the improved “phase_field” model of TrioCFD code. Such a model can solve several equations of Cahn-Hilliard coupled with Navier-Stokes equations to treat coupled mass transfer and hydrodynamic phenomena. To illustrate both the capacity of the model to solve such problem and the interest of fully coupled simulations we have considered the case of a multicomponent droplet rising and sinking in water. The relative importance of advection and diffusion is a key parameter in this phenomenon. Accordingly, we have carried out a study with different mobilities in order to understand how the diffusion layer is affected by the flow. In our case of study where the flow is buoyancy driven, the effects of considering a fully coupled system go far beyond a correction of the parameters of a simplified model. Indeed, the coupling between the

flow and the diffusion leads to a significant increase in the magnitude of the upward motion of the droplet before it starts to fall. The analysis of our results allows us to link this phenomenon with a drag effect of the light diffusion layer around the droplet.

Hence in this work we have shown that the use of fully coupled models for the evolution of multiphase flows can be necessary as soon as there is a significant diffusion from one phase to the other. This is typically the case in many multicomponent systems. This work can find applications in many other fields of application ranging from the study of phase inversion of the corium pool and CO₂ sequestration in deep aquifers to microfluidic devices.

ACKNOWLEDGMENTS

We would like to thank Elie Saikali from Université Paris-Saclay, CEA, Service de Génie Logiciel pour la Simulation, for his support in the development of the TrioCFD code for this work.

DATA AVAILABILITY STATEMENT

AIP Publishing believes that all datasets underlying the conclusions of the paper should be available to readers. Authors are encouraged to deposit their datasets in publicly available repositories or present them in the main manuscript. All research articles must include a data availability statement stating where the data can be found. In this section, authors should add the respective statement from the chart below based on the availability of data in their paper.

-
- [1] R. Zanella, R. Le Tellier, M. Plapp, G. Tegze, and H. Henry, “Three-dimensional numerical simulation of droplet formation by Rayleigh–Taylor instability in multiphase corium,” *Nuclear Engineering and Design* **379**, 111177 (2021).
 - [2] V. G. Asmolov, S. S. Abalin, Yu. A. Veselkin, V. Yu. Vishnevsky, V. V. Vlasov, B. L. Gershman, Yu. G. Degaltsev, Ye. K. Dyakov, J. F. Isaev, A. N. Kiselev, N. P. Kiselev, A. M. Kovalev, A. G. Ol’khovsky, K. V. Pechalin, L. M. Semenov, V. F. Strizhov, T. V. Trushkina, V. S. Uglov, Yu. M. Utkin, V. V. Chudanov, A. E. Aksenova, V. A. Pervichko, and L. M. Khazanivich, *RCW Post-Test Analysis Results*, Technical Report MP-TR-11 (Russian Research Centre Kurchatov Institute, 2003).
 - [3] M. Barrachin and F. Defoort, “Thermophysical Properties of In-Vessel Corium: MASCA Programme Related Results,” in *Proc. of MASCA Seminar* (OECD, Aix-en-Provence, France, 2004).
 - [4] Shuheng Zhang, Charline J.J. Gerard, Aziza Ikni, Gilles Ferry, Laurent M. Vuillard, Jean A. Boutin, Nathalie Ferte, Romain Grossier, Nadine Candoni, and Stéphane Veesler, “Microfluidic platform for optimization of crystallization conditions,” *Journal of Crystal Growth* **472**, 18–28 (2017), industrial Crystallization and Precipitation in France (CRISTAL-8), May 2016, Rouen (France).
 - [5] G.P.D. De Silva, P.G. Ranjith, and M.S.A. Perera, “Geochemical aspects of co₂ sequestration in deep saline aquifers: A review,” *Fuel* **155**, 128–143 (2015).
 - [6] Zheming Zhang and Ramesh Agarwal, “Numerical simulation and optimization of co₂ sequestration in saline aquifers,” *Computers & Fluids* **80**, 79–87 (2013), selected contributions of the 23rd International Conference on Parallel Fluid Dynamics ParCFD2011.
 - [7] M. Wegener, N. Paul, and M. Kraume, “Fluid dynamics and mass transfer at single droplets in liquid/liquid systems,” *International Journal of Heat and Mass Transfer* **71**, 475–495 (2014).

- [8] Abhijit Rao, Rupesh K. Reddy, Kalliat T. Valsaraj, Krishnaswamy Nandakumar, Shashank Pandey, and Chunliang Wu, "Influence of unsteady mass transfer on dynamics of rising and sinking droplet in water: Experimental and CFD study," *AIChE Journal* **61**, 342–354 (2015).
- [9] W. F. Noh and Paul Woodward, "Slic (simple line interface calculation)," in *Proceedings of the Fifth International Conference on Numerical Methods in Fluid Dynamics June 28 – July 2, 1976 Twente University, Enschede*, edited by Adriaan I. van de Vooren and Pieter J. Zandbergen (Springer Berlin Heidelberg, Berlin, Heidelberg, 1976) pp. 330–340.
- [10] S. Mirjalili and S.S. Jain and M.S. Dodd, *Interface-capturing methods for two-phase flows: An overview and recent developments.*, Annual Research Briefs (Center For Turbulence Research, U. Stanford, 2017).
- [11] D. M. Anderson, G. B. McFadden, and A. A. Wheeler, "A Phase-Field Model of Solidification with Convection," *Physica D* **135**, 175–194 (2000).
- [12] R. Folch and M. Plapp, "Quantitative phase-field modeling of two-phase growth," *Physical Review E* **72**, 011602 (2005).
- [13] John W Cahn and John E Hilliard, "Free Energy of a Nonuniform System. I. Interfacial Free Energy," *The Journal of Chemical Physics* **28**, 258–267 (1958).
- [14] Junseok Kim and John Lowengrub, "Phase field modeling and simulation of three-phase flows," *Interfaces and Free Boundaries* , 435–466 (2005).
- [15] Gyula I. Tóth, Mojdeh Zarifi, and Bjørn Kvamme, "Phase-field theory of multicomponent incompressible Cahn-Hilliard liquids," *Physical Review E* **93**, 013126 (2016).
- [16] F. Magaletti, F. Picano, M. Chinappi, L. Marino, and C. M. Casciola, "The sharp-interface limit of the Cahn–Hilliard/Navier–Stokes model for binary fluids," *Journal of Fluid Mechanics* **714**, 95–126 (2013).
- [17] R. Zanella, G. Tegze, R. Le Tellier, and H. Henry, "Two- and three-dimensional simulations of Rayleigh–Taylor instabilities using a coupled Cahn–Hilliard/Navier–Stokes model," *Physics of Fluids* **32** (2020), 10.1063/5.0031179.
- [18] Hyun Geun Lee, Junxiang Yang, Sangkwon Kim, and Junseok Kim, "Modeling and simulation of droplet evaporation using a modified Cahn–Hilliard equation," *Applied Mathematics and Computation* **390**, 125591 (2021).
- [19] Yannis Vasilopoulos, "An alternative phase-field interfacial tension force representation for binary fluid systems," *Physics of Fluids* **32**, 102101 (2020).
- [20] Douglas R. Tree, Kris T. Delaney, Hector D. Ceniceros, Tatsuhiro Iwama, and Glenn H. Fredrickson, "A multi-fluid model for microstructure formation in polymer membranes," *Soft Matter* **13**, 3013–3030 (2017).
- [21] M.A. Rasolofomanana, C. Cardon, M. Plapp, T. Philippe, H. Henry, and R. Le Tellier, "Diffuse-interface modelling of multicomponent diffusion and phase separation in the U-O-Zr ternary system," *Computational Materials Science* **214** (2022), 10.1016/j.commatsci.2022.111650.
- [22] C. Cardon, R. Le Tellier, and M. Plapp, "Modelling of liquid phase segregation in the Uranium–Oxygen binary system," *CALPHAD ; computer coupling of phase diagrams and thermochemistry* **52**, 47–56 (2016).
- [23] J S Rowlinson, "Translation of J. D. van der Waals' "The Thermodynamic Theory of Capillarity Under the Hypothesis of a Continuous Variation of Density";" *Journal of Statistical Physics* **20**, 197–200 (1979).
- [24] Joseph B. Collins and Herbert Levine, "Diffuse interface model of diffusion-limited crystal growth," *Phys. Rev. B* **31**, 6119–6122 (1985).
- [25] Gunduz Caginalp and Paul Fife, "Phase-field methods for interfacial boundaries," *Phys. Rev. B* **33**, 7792–7794 (1986).
- [26] Hao Wu, "A Review on the Cahn-Hilliard Equation: Classical Results and Recent Advances in Dynamic Boundary Conditions," *Electronic Research Archive* **30**, 2788–2832 (2022), arxiv:2112.13812 [math].
- [27] Sourabh B. Kadambi, Fadi Abdeljawad, and Srikanth Patala, "A phase-field approach for modeling equilibrium solute segregation at the interphase boundary in binary alloys," *Computational Materials Science* **175**, 109533 (2020).
- [28] C. Cardon, R. Le Tellier, and M. Plapp, "Modelling of Liquid Phase Segregation in the Uranium-Oxygen Binary System," *CALPHAD: Computer Coupling of Phase Diagrams and Thermochemistry* **52**, 47–56 (2016).
- [29] S Mirjalili, S S Jain, and M S Dodd, "Interface-capturing methods for two-phase flows: An overview and recent developments," *Center for Turbulence Research Annual Research Briefs* , 117–135 (2017).
- [30] Junseok Kim, "Phase-Field Models for Multi-Component Fluid Flows," *Communications in Computational Physics* **12**, 613–661 (2012).
- [31] CEA, "TrioCFD," <https://github.com/cea-trust-platform/TrioCFD-code> (2021-2023).

- [32] Pierre-Emmanuel Angeli, Ulrich Bieder, and Gauthier Fauchet, “Overview of the TRIOCFD Code,” in *NURETH-16* (Chicago, USA, 2015).
- [33] M. A. Rasolofomanana, R. Le Tellier, and H. Henry, “Two-dimensional Numerical Simulation of Rayleigh-Taylor Instabilities in Immiscible Fluids using the Phase-Field Model of TrioCFD Code,” in *NUTHOS-13* (Taiwan, 2022).
- [34] No slip boundary conditions were imposed through a diffuse boundary approach.
- [35] R. Zanella, G. Tegze, M. Plapp, R. Le Tellier, and H. Henry, “Numerical Simulation of Droplet Formation by Rayleigh-Taylor Instability in Multiphase Corium,” in *Proc. of International Topical Meeting on Advances in Thermal Hydraulics ATH’2020* (Palaiseau, France, 2020).
- [36] R. Clift, Grace, J.R., and Weber, M., “Bubbles, Drops and Particles,” Academic Press (1978).
- [37] This is expected in an infinite domain with a finite size droplet and the thermodynamic landscape used here.
- [38] Marco Belloli, Stefano Giappino, Fabio Robustelli, and Claudio Somaschini, “Drafting Effect in Cycling: Investigation by Wind Tunnel Tests,” *Procedia Engineering* **147**, 38–43 (2016).
- [39] Massimo Marro, Jack Leckert, Ethan Rollier, Pietro Salizzoni, and Christophe Bailly, “Wind tunnel evaluation of novel drafting formations for an elite marathon runner,” *Proceedings of the Royal Society A: Mathematical, Physical and Engineering Sciences* **479**, 20220836 (2023).